Element-selective structural visualization for the oxygen-induced surface of Nb(110)

Yuuki Yasui,[1,*] Katsuyuki Matsunaga,[2,3] Keisuke Sagisaka,[4] and Yoshiaki Sugimoto[1,†]
[1]*Department of Advanced Materials Science, The University of Tokyo, Kashiwa, Chiba 277-8561, Japan*
[2]*Department of Materials Physics, Nagoya University, Furo-cho, Chikusa, Nagoya 464-8603, Japan*
[3]*Nanostructures Research Laboratory, Japan Fine Ceramics Center, 2-4-1 Mutsuno, Atsuta, Nagoya 456-8587, Japan*
[4]*Center for Basic Research on Materials, National Institute for Materials Science, 1-2-1 Sengen, Tsukuba, Ibaraki 305-0047, Japan*

(Received 7 September 2023; revised 2 February 2024; accepted 9 April 2024; published 8 May 2024)

The highest superconducting transition temperature in Nb among elemental materials facilitates applications of superconducting junctions. Nonetheless, its surface forms self-organized oxide structures, which hinders the preparation of well-defined interfaces. We investigated the atomic structure of oxygen-induced Nb(110) surfaces, aiming to define the substrates for such interfaces. The atomic force microscopy and scanning tunneling microscopy measurements visualized two rows of apparently low-lying Nb and three rows of O between Nb chains. An optimized model structure is proposed based on density-functional theory calculations. Analysis of the Bader charge and the density of states clarified how the atoms appear in the microscopies.

DOI: 10.1103/PhysRevB.109.195417

I. INTRODUCTION

Niobium has the highest superconducting transition temperature among elemental metals without the application of high pressure, which promotes applications such as tunneling junctions between a normal metal and a superconductor [1–3] and Josephson junctions between superconductors [4–8]. Though their interfacial conditions are crucial to determine the junction properties [9,10], the affinity of Nb to oxygen burdens the preparation of well-defined interfaces.

The surface of Nb is covered with oxide layers even in ultra-high vacuum (UHV) conditions. The oxide layer cannot be removed with standard cleaning methods [11], because O atoms segregate from the bulk to the surface at annealing [12]. Recently, methods to prepare clean surfaces were reported. Clean surfaces of Nb(110) are achieved by annealing in UHV at 2410 °C, that is, only 70 °C below its melting point [12]. Hydrogen treatments and additional annealing at 1000 °C are required for clean Nb(111) surfaces [13]. Such sophisticated preparation methods, however, may not be preferred for the device fabrication process. We could instead make use of the oxidized surface of Nb for more practical applications by resolving its properties in detail.

The structure of the oxide surface of Nb(110) has been intensively studied. When the crystal is annealed below 145 °C in an UHV condition, Nb_2O_5 dominates in the surface oxide layer, and NbO_2 dominates below 300 °C [14,15]. NbO is formed with annealing at even higher temperatures. In the range of 927 °C–1927 °C, no significant change was detected in the surface NbO structure [16]. Scanning tunneling microscopy (STM) observations reported Nb atoms form a quasiperiodic chain structure and are referred to as Nb* chains [12,16–23]. Several models have been proposed so far [16,23,24] based on x-ray photoelectron spectroscopy (XPS) [21,24–27], x-ray reflectivity [15], low-energy electron diffraction [11,14,28,29], Auger electron spectroscopy [14,29], and electron energy loss spectroscopy [14]. These models are constructed by combining the bulk Nb(110) and the bulk NbO(111) structures and by putting Nb adatoms to reproduce the Nb* chain structure. A more recent investigation raised a question on the Nb* adatom structure [30].

Here, we performed noncontact atomic force microscopy (AFM) on NbO/Nb(110) surfaces. The AFM technique is suited for structural identification [31–34]. Nb and O atoms are visualized independently by using different tip states, and the surface atomic arrangements are clarified. A comparison of AFM and STM shows the relative position of Nb and O atoms. A surface model is proposed based on density-functional-theory (DFT) calculations, which is consistent with the AFM and STM observations. The Bader charge and the density of states (DOS) analysis further explain why AFM and STM visualize atoms differently and why the apparent height does not necessarily represent the atomic height.

II. METHODS

Nb single crystals with a purity of better than 99.99% were purchased from MaTecK. Several cycles of Ar^+ ion sputtering (1.3×10^{-3} Pa, 4 keV, 20 min) and annealing at 1200 °C were carried out in UHV chambers ($\sim 10^8$ Pa) to get rid of impurities. Annealing at 1200 °C for 1 min in UHV conditions makes the oxygen-induced surface structure.

AFM measurements at room temperature were performed with a Unisoku custom-built AFM/STM system [35]. Si cantilevers with and without a Pt coating were used after cleaning with Ar^+ ion sputtering. Since the tips often contact with the sample surfaces, it is assumed that the tips are covered with materials from the sample surfaces. The resonance fre-

---

[*] yasui@k.u-tokyo.ac.jp
[†] ysugimoto@k.u-tokyo.ac.jp

quencies of the cantilevers with and without a Pt coating are around 167 kHz and 157 kHz, and the spring constants are around 38 N/m and 30 N/m, respectively. The oscillation of the cantilever was monitored with an optical interferometer. Measurements at helium temperature were performed with a Unisoku custom-built scanning probe microscope with the Kolibri sensor [36]. The resonance frequency is around 1 MHz, and the effective spring constant is around 1.3 MN/m. All the measurements were operated with the frequency-modulation mode. For the constant-frequency-shift topographic images, the sample bias voltage was adjusted to compensate for the contact potential difference between the tip and the sample. The dI/dV conductance was measured with a standard lock-in technique.

DFT calculations were carried out with the projector augmented wave (PAW) method involved in the VASP program [37,38]. The generalized gradient approximation (GGA) and the exchange-correlation functional parameterized by Perdew, Burke, and Ernzerhof (PBE) [39] were used. In the PAW potentials, $4p$, $4d$, and $5s$ orbitals for niobium and $2s$ and $2p$ orbitals for oxygen were considered as valence electrons. Electronic wave functions were expanded by plane waves up to a cutoff energy of 400 eV. Atomic positions in the bcc-Nb unit cell and surface supercells (described below) were optimized until their forces became less than 0.1 eV/nm.

For calculations of the Nb(110) surface, periodic supercells containing atomic Nb(110) slabs with a vacuum layer were initially constructed. A thickness of the vacuum layer was set at 1 nm for the structural optimization and the DOS calculation, so as to prevent any spurious interactions between the surfaces at both ends of the slab. In order to obtain structurally optimized Nb(110) surfaces, Nb(110) slabs were initially cut out of bulk Nb. In the structural optimization, Nb atoms in the two atomic layers from one slab surface were fixed and all other atoms were relaxed with the same convergence criterion as that for bulk, described above. From calculations of the different-sized Nb(110) slabs, the slab thickness was determined to be eleven atomic layers so that the Nb(110) interlayer distance between the central Nb layers matches the bulk value. In this case, Brillouin zone integration was performed with a Γ-centered $5 \times 5 \times 1$ k-point mesh [12].

As can be seen in the Results section, a periodic Nb* chain structure was observed. According to the distance between the Nb* chains (around 1.1 nm), different surface supercells were generated by a four-times extension of the minimum unit of Nb(110) toward the $[\bar{1}1\bar{1}]$ direction (see Fig. 4). In this case, a $5 \times 1 \times 1$ mesh was used for k-point sampling.

Additional O atoms in the surface layer were also considered. O atoms were introduced at half of the hollow sites of Nb atoms just below the topmost Nb layer because the thickness of the surface oxide layer was estimated to be 1.4 monolayers [16], 1–2 atomic layers [26], or 500 pm [23,24]. From the total energies of the O-induced supercells with different O configurations as a function of the oxygen chemical potential, the most stable O configuration was determined. Removal of Nb and O atoms from the extended supercells was also assumed to validate the observations, which will be discussed later.

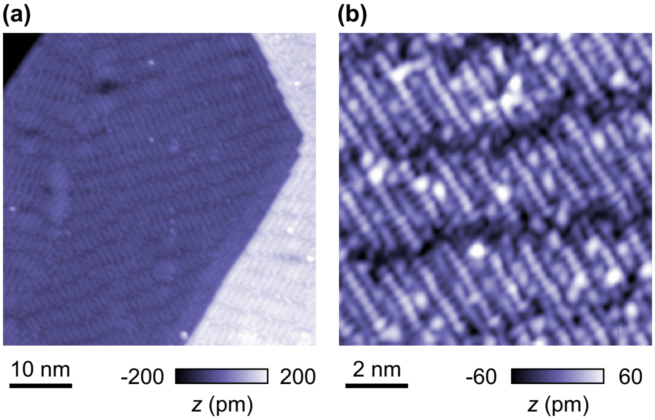

FIG. 1. Constant-current STM topographic images taken at temperature $T = 5$ K. (a) A large field-of-view image. The sample bias voltage $V_s = -10$ mV, current setpoint $I_s = -10$ pA, and oscillation amplitude $A = 90$ pm. (b) A magnified image with resolution of the Nb* chain atoms. $V_s = -10$ mV, $I_s = -100$ pA, $A = 0$ pm.

The STM image and conductance spectrum are simulated based on the Tersoff-Hamann method [40,41] implemented in the BSKAN code [42]. The cut-off energy is 400 eV, thickness of the vacuum in the slab is 1.5 nm, the number of k points is $21 \times 21 \times 1$, and the sample bias voltage is -10 mV.

III. RESULTS

The surface morphology was checked with STM to compare the sample with the previous reports. A large field-of-view image shows step and terrace structures [Fig. 1(a)]. The angle between the two steps is around 110°, resulting from the $\langle 111 \rangle$ directions of the (110) surface. The Nb* chain structures run almost parallel to the step edges and form domains for both directions of the step edges.

The Nb* chain atoms are resolved in a magnified view as in Fig. 1(b). The chain is constituted of around ten atoms with a chain-to-chain distance of 1.1 nm. In our STM observations, atoms were observed only in the chain structure, and atoms were not clearly observed between the chains. The chain structure was observed for any bias voltage within ±1 V. These features are consistent with the previously reported STM observations [12,16–19,21–23].

AFM observations give further information on the surface atomic structure. Two modes of atomic resolutions were obtained depending on the tip conditions. In Fig. 2(a) a quasiperiodic chain structure is observed, which is constituted of around ten atoms. The distance between the chains is around 1 nm. These values are similar to the Nb* chain structure observed in STM, and thus we consider that Nb atoms are observed in this imaging mode. Furthermore, atoms between the chains are resolved as in the magnified view in Fig. 2(b). Interestingly, an additional two rows of Nb atoms are located at apparently low positions. These atoms have not been revealed in the STM measurements. A line profile highlights its periodicity: one Nb* row and two low-lying Nb rows [Fig. 2(c)]. The difference in the apparent height between the Nb* chain and the lower Nb is merely 20 pm, which suggests that the lower Nb atoms are not located in the

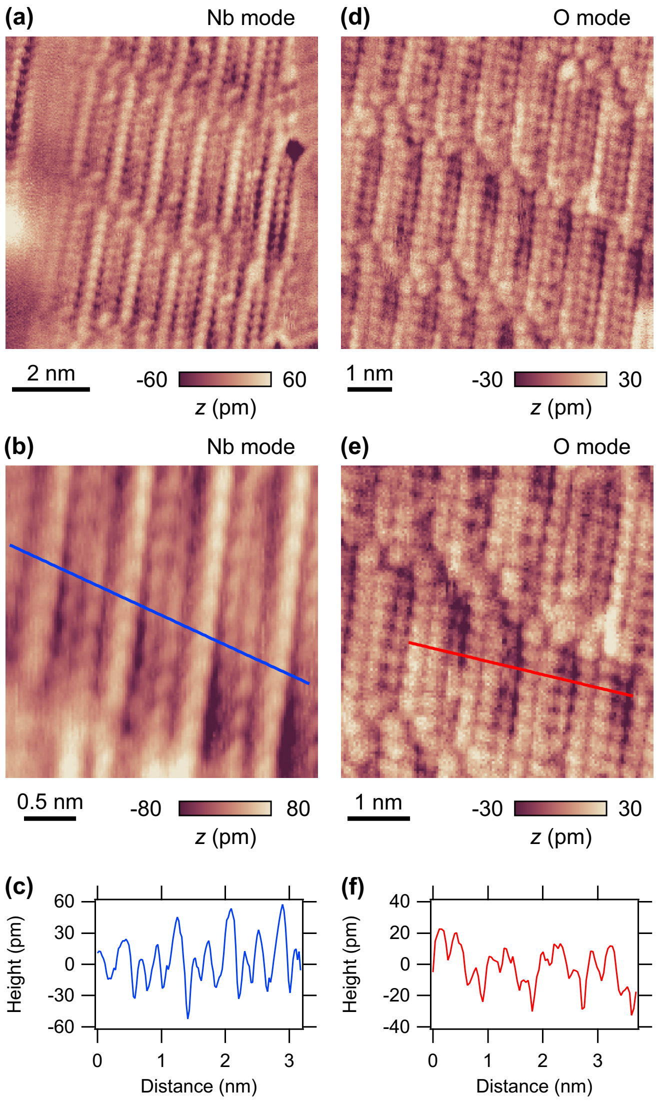

FIG. 2. Constant-frequency-shift AFM topographic images taken at $T \sim 300$ K. (a) Nb* chain structure in Nb mode imaging. $V_s = 300$ mV, the frequency-shift setpoint $\Delta f_s = -1.7$ Hz, $A = 20$ nm. (b) A magnified view with atomic resolution to apparently low-lying Nb atoms. $V_s = 100$ mV, $\Delta f_s = -8.0$ Hz, $A = 20$ nm. (c) A line profile of (b). (d) A quasiperiodic structure in O-mode imaging. $V_s = 900$ mV, $\Delta f_s = -217$ Hz, $A = 5$ nm. (e) A magnified view, where three O rows are resolved. $V_s = 900$ mV, $\Delta f_s = -227$ Hz, $A = 5$ nm. (f) A line profile of (e). The bias voltages are adjusted to compensate for the contact potential difference between the tips and the samples.

underlying layer. We refer to these apparently low-lying Nb atoms as Nb-1 and Nb-2.

For a different imaging mode, another structure was visualized at a different area of the sample as in Figs. 2(d)–2(f). We consider that the other elements, namely, O atoms, are visualized. In this visualization mode, the quasiperiodicity is consistent with that for the Nb mode: around 10 atoms in length and 1 nm in width. Importantly, three rows of O form a unit of quasi-repetition, and each row has nearly the same number of atoms. The height in these rows appears within 30 pm, suggesting these rows are located nearly in the same plane.

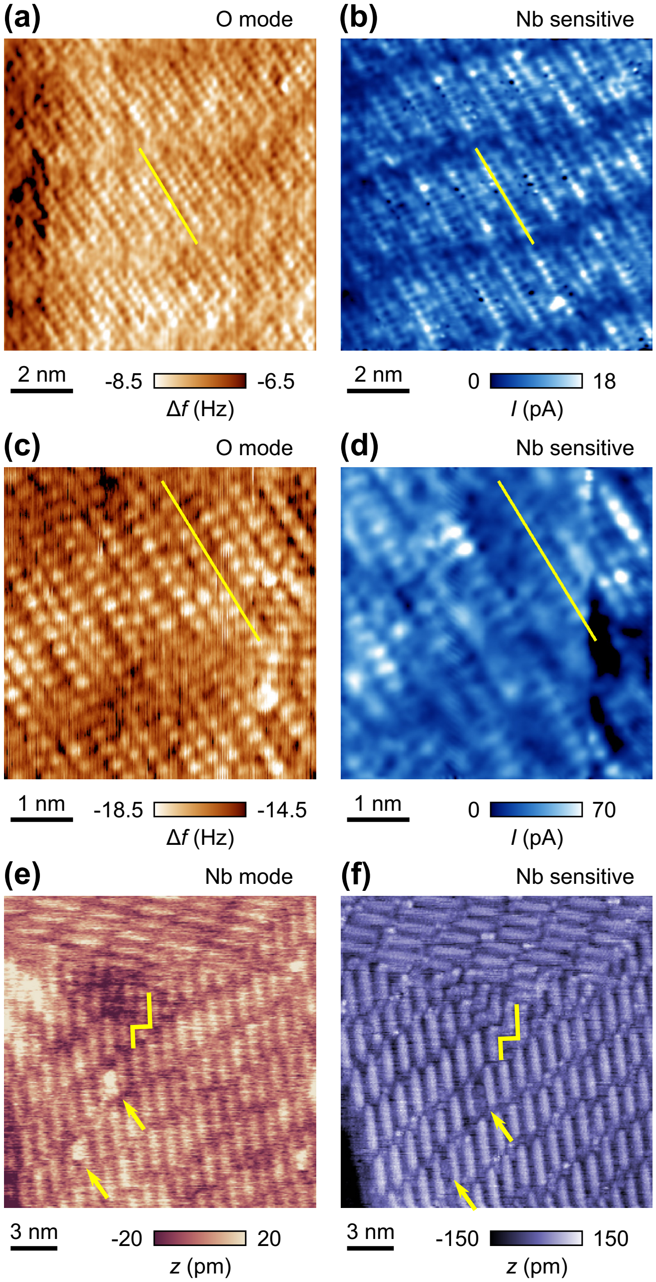

FIG. 3. Correspondence of AFM and STM visualized atomic positions. (a) A frequency-shift image during a constant-height scan. The image is low-pass Fourier filtered. (b) Simultaneously obtained current image with Fourier low-pass filter. (c) A raw frequency-shift image at a constant-height scan. (d) Simultaneously obtained current image with low-pass Fourier filter. Yellow lines highlight the positions of Nb* chains in current images, and the same pixels are also marked in the frequency-shift images. For (a)–(d), $V_s \sim 1$ μV, $A = 90$ pm, $T = 5$ K. (e) Constant-frequency-shift AFM topographic image. $V_s = -200$ mV, $\Delta f_s = -5.1$ Hz, $A = 20$ nm, $T \sim 300$ K. (f) Constant-current topographic image in the same field of view. $V_s = -2000$ mV, $I_s = -30$ pA, $A = 20$ nm, $T \sim 300$ K. Impurities are marked with yellow arrows for references to the position.

Such element-selective imaging is reported in other materials such as CaF_2 [43–45], TiO_2 [46–48], $MgAl_2O_4$ [49,50], oxygen-terminated Cu [51], and $SrTiO_3$ [52]. This is interpreted as follows. The constant-frequency-shift feedback is maintained in the attractive force region. Each element in the sample is charged in opposite polarity due to the difference in the electronegativity. When the electrostatic force dominates the tip-sample interaction, one of the elements can provide an attractive force depending on the charge state of the tip. Therefore, the tip termination polarity determines which element is to be detected. We consider that a similar mechanism is applied to the NbO/Nb(110) surfaces.

Relative positions of Nb and O atoms are determined by simultaneous measurements of AFM and STM. The frequency-shift images visualize the O atoms [Figs. 3(a) and 3(c)], while the current images represent the position of Nb* chain atoms [Figs. 3(b) and 3(d)]. Positions of Nb* chains are marked with yellow lines in Figs. 3(b) and 3(d). Corresponding pixels are also marked to compare in Figs. 3(a) and 3(c). The Nb* chains appear in the valley between the bunches of three O rows. There is a slight shift (∼70 pm) away from the center of the valley.

Comparison in the Nb mode is shown in Figs. 3(e) and 3(f). These images are taken separately in the same field of view. The positions can be compared by referring to impurities marked with arrows. These impurities are located in between the chains for both AFM and STM images. Thus, the chain structure in Nb-mode AFM detects the same Nb* chains seen in STM.

To summarize the AFM observations, two rows of apparently low-lying Nb atoms and three rows of O atoms are found between the Nb* chains. In previous studies, the surface oxide structure had been constructed by a combination of the bulk Nb(110) and the bulk NbO(111). However, the ideal surface of NbO(111) cannot explain the present AFM observations for the following reasons. Firstly, the bulk NbO(111) structure expects three Nb rows between Nb* chains. Secondly, the number of O atoms in each row is not uniform due to the kagome structure of NbO(111). Thirdly, the Nb* chains were placed on top of the NbO layer as adatoms, but the protrusion may be too high to explain the observation.

IV. DISCUSSION

A simple combination of the bulk Nb(110) and the bulk NbO(111) may not be sufficient for a more realistic model. To get further insight into the O-induced surface structure of Nb(110), we performed DFT calculations of the O-induced Nb(110) supercells extended by four times toward the $[\bar{1}1\bar{1}]$ direction (see Sec. II). The initial states contain O atoms stuffed in the surface layer of Nb(110). Since such a surface is subjected to compressive stress due to oxygen inclusion, removal of pairs of Nb and O in the surface layer was assumed. All possible combinations of removal were calculated, and the most stable atomic structure obtained after structure optimization is shown in Fig. 4. The calculated structure captures the basic periodicity in the AFM observations. The Nb* chains (colored in blue) run along the $[\bar{1}11]$ direction, where the distance between the chains is 1.17 nm. Two Nb rows (colored in green) and three O rows (colored in red and orange) are located between the Nb* chains. Nb atoms are aligned almost parallel to the $[\bar{1}1\bar{1}]$ direction, and O atoms are aligned close

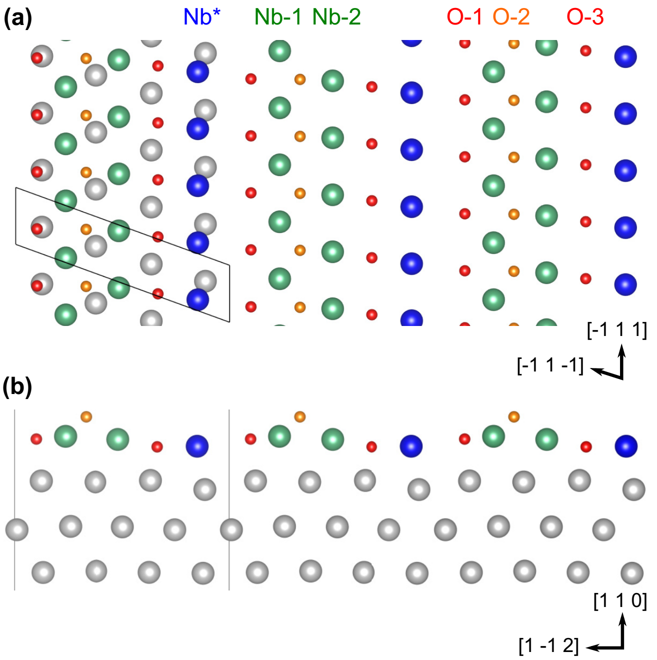

FIG. 4. A DFT-optimized model structure. (a) Top view. The second Nb layer is depicted only on the left-hand-side column. (b) Side view. Blue, Nb* chain atoms; green, apparently low-positioned Nb atoms; gray, bulk Nb atoms; red/orange, O atoms. The parallelogram in gray depicts the cell for the calculation.

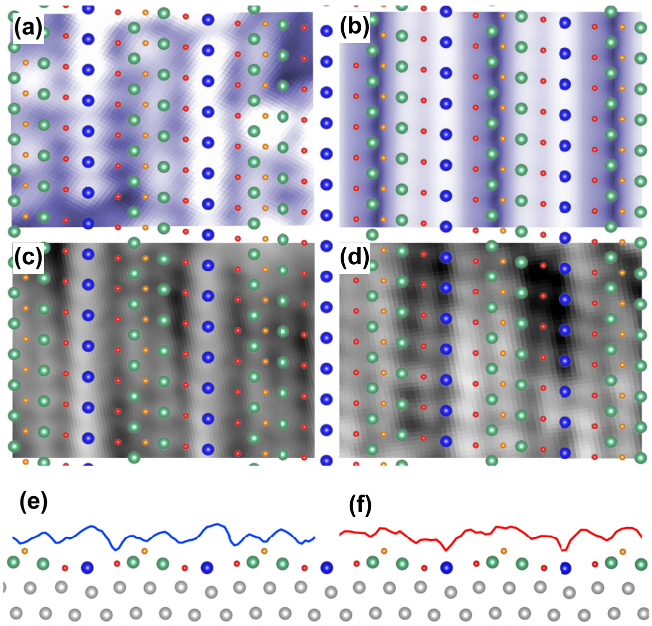

FIG. 5. Comparison of the experimental observations and the model. (a) STM topographic image [Fig. 1(b)]. (b) Simulated STM image for $V_s = -10$ mV. (c) AFM topographic image in Nb mode [Fig. 2(b)]. (d) AFM topographic image in O mode [Fig. 2(e)]. (e), (f) AFM line profiles [Figs. 2(c) and 2(f)]. Images in (c) and (d) are processed with Fourier low-pass filters and affine corrections. The z direction of the AFM line profiles are scaled by factors of (e) 5 and (f) 15.

TABLE I. Parameters obtained for the present structural model.

	Nb*	Nb-1	Nb-2	O-1	O-2	O-3
Bader charge	+0.54	+1.41	+0.74	–1.22	–1.17	–1.24
DOS at E_F	0.96	0.56	0.73	0.06	0.07	0.08
Relative height (pm)	0	51	35	37	151	–3

to the $[1\bar{1}2]$ direction. A comparison of the model and AFM images is illustrated in Figs. 5(c) and 5(d).

The height profile of the model can be compared with the line profiles in AFM, as shown in Figs. 5(e) and 5(f). In the AFM observation, three O rows appear in similar heights. In contrast, the model expects that O-2 locates 114 pm and 154 pm higher than O-1 and O-3, respectively. AFM topographic images detect the charge state, and hence the Bader-charge analysis [53], which approximates the charge state of each atom, helps to interpret the observations. We found that O-2 has a smaller charge than O-1 and O-3 (Table I). That reduces the height difference in AFM feedback. On the other hand, the value of the Bader charge alone cannot explain why the Nb* atoms appear higher in the AFM. We speculate that the Nb* atoms are exposed to the vacuum, while Nb-1 and Nb-2 atoms are partly covered with O atoms. Thus, the charge of Nb-1 and Nb-2 is screened with surrounding O atoms, leaving the unscreened Nb* atoms apparently high.

Let us compare the model with the STM observations. STM topographic images detect the DOS integrated from the Fermi level E_F to V_s, on top of atomic corrugations. Hence, the DOS at E_F simulates how atoms appear in STM topographic images. We calculated the DOS for the present structure as shown in Table I. The Nb* has larger DOS than those of Nb-1 and Nb-2, and thus the Nb* chains appear higher in the STM measurements. Besides, the low DOS of O atoms explains why O atoms are not detected with STM.

The present model is further supported by comparing the observed STM topographic image with a simulated STM image as in Figs. 5(a) and 5(b). Nb* appears most strongly in the simulated image, as expected from the large DOS at E_F. Nb-2 appears very weakly in the simulated image. This rationalizes the weak signal between Nb* chains. Nb-1 hardly appears in the simulation, as its low DOS implies.

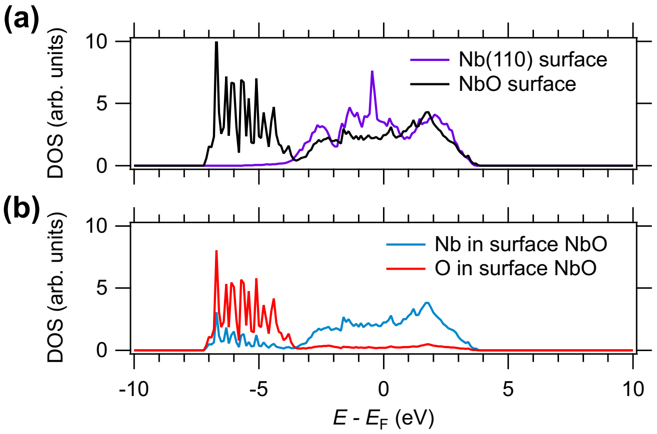

FIG. 6. DOS calculated for the present model. (a) Effect of the surface oxidization. (b) Contribution from the surface Nb and O atoms.

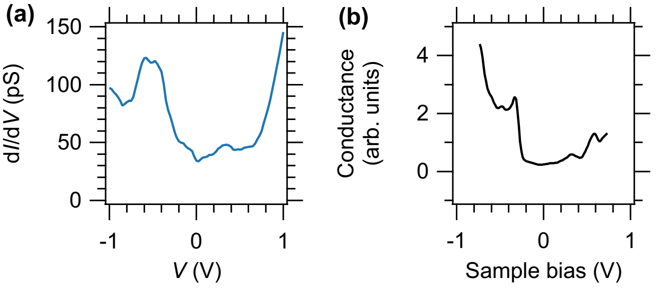

FIG. 7. (a) A measured dI/dV curve. $V_s = -1$ V, $I_s = -100$ pA, bias modulation amplitude $V_{mod} = 25$ mV, bias modulation frequency $f_{bias} = 617.3$ Hz, $A = 0$ pm, and $T = 5$ K. (b) A simulated conductance curve at 400 pm above Nb*.

We calculated the DOS for the present oxide surface model (Fig. 6). The peak structure at −450 mV in the clean Nb(110) surface originates from the Nb $4d_{z^2}$ orbital. The peak is suppressed in the oxide surface. Figure 6(b) shows the projected DOS for each element at the surface. The DOS near E_F is mostly contributed from Nb 4*d* orbitals. O 2*p* orbitals appear mainly from −7 eV to − 4 eV. Figure 7(a) shows a measured tunneling conductance spectrum, which is approximately proportional to the DOS. The observed dI/dV curve reproduces the previous report [30], where a characteristic peak is obtained at −450 mV. The peak is reproduced with a simulation of tunneling conductance at 400 pm above the Nb* atom [Fig. 7(b)]. The consistency further supports the present model.

In the present model, the quasiperiodic structure including the finite length of Nb* chains is not obtained because of the limitation in the cell size for the calculation. We consider that the relaxation from the compressive strain coming from extra O inclusion causes the quasiperiodic structure, similar to the case in N-adsorbed Cu(001) surfaces [54]. This may also cause the rotation of Nb* chains by 5° with respect to the [111] direction as reported in Ref. [23]. This also limits the discussion of the global symmetry of the surface, and hence we cannot make a conclusion about the Nishiyama-Wasserman epitaxial relationship proposed in previous reports [18,22].

We also discuss the present model by referring to previous reports. Photoelectron spectroscopy studies estimate the ratio of Nb and O is close to 1:1 in the topmost layer [16,19]. The present model holds this condition. An XPS experiment concluded that there are two oxygen chemical states, chemisorbed oxygen and oxygen entering into NbO_x clusters, with the ratio of 2 : 1 [21]. We speculate that the O atoms observed in AFM belong to the chemisorbed state and that sparse O inclusions near the surface might belong to the other oxygen state.

V. CONCLUSION

Using the noncontact AFM technique, elements were selectively imaged in atomic resolution in the oxygen-induced surface structure of Nb(110). This suggests that two rows of Nb atoms and three rows of O atoms are located between the

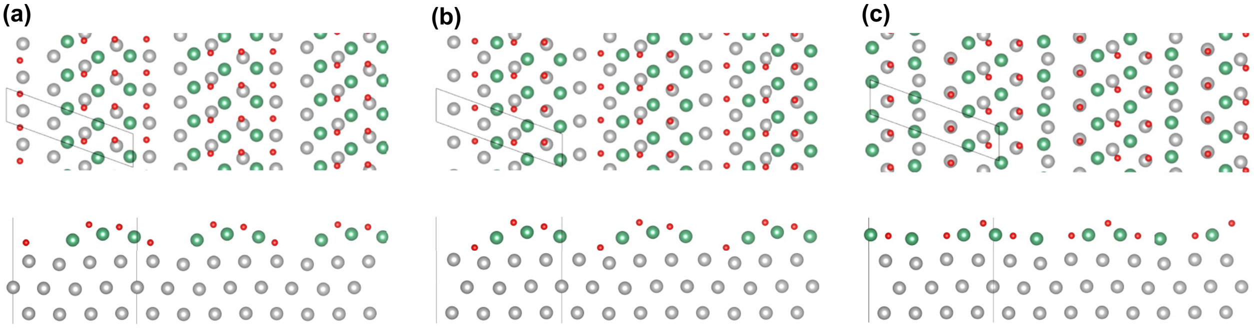

FIG. 8. DFT-optimized structural models from different initial states. The total energy for the model in Fig. 4 is −458.19 eV. The total energies are (a) −458.07 eV, (b) −458.16 eV, and (c) −458.11 eV.

Nb* chains. Based on DFT calculations, a surface model is proposed. The Bader-charge and the DOS calculations simulate why the apparent height in AFM and STM does not necessarily represent the atomic height. The present results may pave a way for using the self-organized oxide surface of Nb as well-defined substrates for superconducting junctions.

ACKNOWLEDGMENTS

The authors acknowledge D. Katsube and Y. Adachi for discussion. This work was supported by Grant-in-Aid JSPS KAKENHI Grants No. 22H04496, No. 20H05849, No. 21K18867, No. 22H05448, and No. 22H01950, by the JST FOREST Program (Grant No. JPMJFR203J, Japan), by the Asahi Glass Foundation, and by the Murata Science Foundation.

APPENDIX

Figure 8 gives references for higher energy states obtained from different initial states. Figure 9 presents a conductance curve representing the superconducting gap observed on the oxide surface.

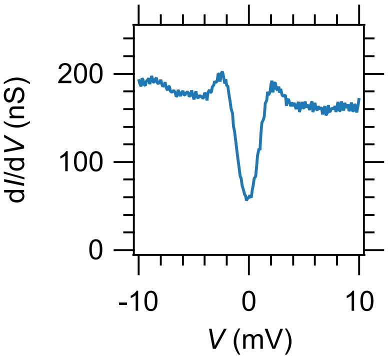

FIG. 9. A dI/dV spectrum showing the superconducting gap observed on the oxide surface. $V_s = -10\,\mathrm{mV}$, $I_s = -1\,\mathrm{nA}$, $V_{\mathrm{mod}} = 0.1\,\mathrm{mV}$, $f_{\mathrm{bias}} = 617.3\,\mathrm{Hz}$, $A = 0\,\mathrm{pm}$, $T = 5\,\mathrm{K}$, and external magnetic field $\mu_0 H = 50\,\mathrm{mT}$.

---

[1] I. Giaever, Energy gap in superconductors measured by electron tunneling, Phys. Rev. Lett. **5**, 147 (1960).

[2] S. H. Pan, E. W. Hudson, and J. C. Davis, Vacuum tunneling of superconducting quasiparticles from atomically sharp scanning tunneling microscope tips, Appl. Phys. Lett. **73**, 2992 (1998).

[3] L. Schneider, P. Beck, J. Wiebe, and R. Wiesendanger, Atomic-scale spin-polarization maps using functionalized superconducting probes, Sci. Adv. **7**, eabd7302 (2021).

[4] B. D. Josephson, Possible new effects in superconductive tunnelling, Phys. Lett. **1**, 251 (1962).

[5] O. Naaman, W. Teizer, and R. C. Dynes, Fluctuation dominated Josephson tunneling with a scanning tunneling microscope, Phys. Rev. Lett. **87**, 097004 (2001).

[6] J. Robinson, J. Witt, and M. Blamire, Controlled injection of spin-triplet supercurrents into a strong ferromagnet, Science **329**, 59 (2010).

[7] D. Vasyukov, Y. Anahory, L. Embon, D. Halbertal, J. Cuppens, L. Neeman, A. Finkler, Y. Segev, Y. Myasoedov, M. L. Rappaport *et al.*, A scanning superconducting quantum interference device with single electron spin sensitivity, Nat. Nanotechnol. **8**, 639 (2013).

[8] Y. Yasui, K. Lahabi, V. F. Becerra, R. Fermin, M. S. Anwar, S. Yonezawa, T. Terashima, M. V. Milošević, J. Aarts, and Y. Maeno, Spontaneous emergence of Josephson junctions in homogeneous rings of single-crystal Sr_2RuO_4, npj Quantum Mater. **5**, 21 (2020).

[9] G. E. Blonder, M. Tinkham, and T. M. Klapwijk, Transition from metallic to tunneling regimes in superconducting microconstrictions: Excess current, charge imbalance, and supercurrent conversion, Phys. Rev. B **25**, 4515 (1982).

[10] J. Brand, P. Ribeiro, N. Néel, S. Kirchner, and J. Kröger, Impact of atomic-scale contact geometry on Andreev reflection, Phys. Rev. Lett. **118**, 107001 (2017).

[11] T. W. Haas, A study of the niobium (110) surface using low energy electron diffraction techniques, Surf. Sci. **5**, 345 (1966).

[12] A. B. Odobesko, S. Haldar, S. Wilfert, J. Hagen, J. Jung, N. Schmidt, P. Sessi, M. Vogt, S. Heinze, and M. Bode, Preparation and electronic properties of clean superconducting Nb(110) surfaces, Phys. Rev. B **99**, 115437 (2019).

[13] J. J. Goedecke, M. Bazarnik, and R. Wiesendanger, STM study of Nb(111) prepared by different methods, Phys. Rev. Mater. **7**, 084803 (2023).

[14] R. Franchy, T. U. Bartke, and P. Gassmann, The interaction of oxygen with Nb(110) at 300, 80, and 20 K, Surf. Sci. **366**, 60 (1996).

[15] M. Delheusy, A. Stierle, N. Kasper, R. P. Kurta, A. Vlad, H. Dosch, C. Antoine, A. Resta, E. Lundgren, and J. Andersen, X-ray investigation of subsurface interstitial oxygen at Nb/oxide interfaces, Appl. Phys. Lett. **92**, 101911 (2008).

[16] I. Arfaoui, J. Cousty, and C. Guillot, A model of the $NbO_{x\approx1}$ nanocrystals tiling a Nb(110) surface annealed in UHV, Surf. Sci. **557**, 119 (2004).

[17] M. Ondrejcek, R. S. Appleton, W. Swiech, V. L. Petrova, and C. P. Flynn, Thermally activated stripe reconstruction induced by O on Nb(011), Phys. Rev. Lett. **87**, 116102 (2001).

[18] C. Sürgers, M. Schöck, and H. v. Löhneysen, Oxygen-induced surface structure of Nb(110), Surf. Sci. **471**, 209 (2001).

[19] I. Arfaoui, J. Cousty, and H. Safa, Tiling of a Nb(110) surface with NbO crystals nanosized by the NbO/Nb misfit, Phys. Rev. B **65**, 115413 (2002).

[20] C. Wolf and U. Köhler, Growth and intermixing of Nb on Fe(110) and Fe on Nb(110), Thin Solid Films **500**, 347 (2006).

[21] A. S. Razinkin, E. V. Shalaeva, and M. V. Kuznetsov, Photoelectron spectroscopy and diffraction of NbO_x/Nb(110) surface, Phys. Met. Metallogr. **106**, 56 (2008).

[22] K. Zhussupbekov, K. Walshe, S. I. Bozhko, A. Ionov, K. Fleischer, E. Norton, A. Zhussupbekova, V. Semenov, I. V. Shvets, and B. Walls, Oxidation of Nb(110): Atomic structure of the NbO layer and its influence on further oxidation, Sci. Rep. **10**, 3794 (2020).

[23] A. S. Razinkin and M. V. Kuznetsov, Scanning tunneling microscopy (STM) of low-dimensional NbO structures on the Nb(110) surface, Phys. Met. Metallogr. **110**, 531 (2010).

[24] M. V. Kuznetsov, A. S. Razinkin, and E. V. Shalaeva, Photoelectron spectroscopy and diffraction of surface nanoscale NbO/Nb(110) structures, J. Struct. Chem. **50**, 514 (2009).

[25] Z. P. Hu, Y. P. Li, M. R. Ji, and J. X. Wu, The interaction of oxygen with niobium studied by XPS and UPS, Solid State Commun. **71**, 849 (1989).

[26] F. Matsui, M. Fujikado, H. Daimon, B. C. Sell, C. S. Fadley, and A. Kobayashi, Structural analysis of oxygen segregated Nb(110) surface by photoelectron diffraction, Czech. J. Phys. **56**, 61 (2006).

[27] A. S. Razinkin, E. V. Shalaeva, and M. V. Kuznetsov, Surface quasi-ordered nanostructures NbO_x/Nb(110): Investigation by surface analysis methods, Bull. Russ. Acad. **72**, 1318 (2008).

[28] T. W. Haas, A. G. Jackson, and M. P. Hooker, Adsorption on niobium (110), tantalum (110), and vanadium (110) surfaces, J. Chem. Phys. **46**, 3025 (1967).

[29] R. Pantel, M. Bujor, and J. Bardolle, Continuous measurement of surface potential variations during oxygen adsorption on the (100), (110) and (111) faces of niobium using mirror electron microscope, Surf. Sci. **62**, 589 (1977).

[30] S. Berman, A. Zhussupbekova, B. Walls, K. Walshe, S. I. Bozhko, A. Ionov, D. D. O'Regan, I. V. Shvets, and K. Zhussupbekov, Unraveling the atomic and electronic structure of nanocrystals on superconducting Nb(110): Impact of the oxygen monolayer, Phys. Rev. B **107**, 165425 (2023).

[31] L. Gross, F. Mohn, N. Moll, P. Liljeroth, and G. Meyer, The chemical structure of a molecule resolved by atomic force microscopy, Science **325**, 1110 (2009).

[32] J. Onoda, L. Feng, K. Yabuoshi, and Y. Sugimoto, Less-ordered structures of silicene on Ag(111) surface revealed by atomic force microscopy, Phys. Rev. Mater. **3**, 104002 (2019).

[33] N. Kawakami, K. Iwata, A. Shiotari, and Y. Sugimoto, Intrinsic reconstruction of ice-I surfaces, Sci. Adv. **6**, eabb7986 (2020).

[34] A. Liebig, C. Setescak, A. Weindl, and F. J. Giessibl, Structural characterization of defects in the topological insulator Bi_2Se_3 at the picometer scale, J. Phys. Chem. C **126**, 21716 (2022).

[35] Y. Sugimoto, Y. Nakajima, D. Sawada, K.-i. Morita, M. Abe, and S. Morita, Simultaneous AFM and STM measurements on the Si(111)-(7 × 7) surface, Phys. Rev. B **81**, 245322 (2010).

[36] Y. Sugimoto and J. Onoda, Force spectroscopy using a quartz length-extension resonator, Appl. Phys. Lett. **115**, 173104 (2019).

[37] P. E. Blöchl, Projector augmented-wave method, Phys. Rev. B **50**, 17953 (1994).

[38] G. Kresse and J. Hafner, *Ab initio* molecular dynamics for open-shell transition metals, Phys. Rev. B **48**, 13115 (1993).

[39] J. P. Perdew, K. Burke, and M. Ernzerhof, Generalized gradient approximation made simple, Phys. Rev. Lett. **77**, 3865 (1996).

[40] J. Tersoff and D. R. Hamann, Theory and application for the scanning tunneling microscope, Phys. Rev. Lett. **50**, 1998 (1983).

[41] J. Tersoff and D. R. Hamann, Theory of the scanning tunneling microscope, Phys. Rev. B **31**, 805 (1985).

[42] W. A. Hofer, Challenges and errors: Interpreting high resolution images in scanning tunneling microscopy, Prog. Surf. Sci. **71**, 147 (2003).

[43] A. S. Foster, C. Barth, A. L. Shluger, and M. Reichling, Unambiguous interpretation of atomically resolved force microscopy images of an insulator, Phys. Rev. Lett. **86**, 2373 (2001).

[44] A. S. Foster, C. Barth, A. L. Shluger, R. M. Nieminen, and M. Reichling, Role of tip structure and surface relaxation in atomic resolution dynamic force microscopy: $CaF_2(111)$ as a reference surface, Phys. Rev. B **66**, 235417 (2002).

[45] S. Fujii and M. Fujihira, Atomic contrast on a point defect on $CaF_2(111)$ imaged by non-contact atomic force microscopy, Nanotechnology **18**, 084011 (2007).

[46] J. V. Lauritsen, A. S. Foster, G. H. Olesen, M. C. Christensen, A. Khnle, S. Helveg, J. R. Rostrup-Nielsen, B. S. Clausen, M. Reichling, and F. Besenbacher, Chemical identification of point defects and adsorbates on a metal oxide surface by atomic force microscopy, Nanotechnology **17**, 3436 (2006).

[47] G. H. Enevoldsen, A. S. Foster, M. C. Christensen, J. V. Lauritsen, and F. Besenbacher, Noncontact atomic force microscopy studies of vacancies and hydroxyls of $TiO_2(110)$: Experiments and atomistic simulations, Phys. Rev. B **76**, 205415 (2007).

[48] G. H. Enevoldsen, H. P. Pinto, A. S. Foster, M. C. R. Jensen, A. Kühnle, M. Reichling, W. A. Hofer, J. V. Lauritsen, and F. Besenbacher, Detailed scanning probe microscopy tip models determined from simultaneous atom-resolved AFM and STM studies of the $TiO_2(110)$ surface, Phys. Rev. B **78**, 045416 (2008).

[49] M. K. Rasmussen, A. S. Foster, B. Hinnemann, F. F. Canova, S. Helveg, K. Meinander, N. M. Martin, J. Knudsen, A. Vlad, E. Lundgren, A. Stierle, F. Besenbacher, and J. V. Lauritsen, Stable cation inversion at the $\mathrm{MgAl_2O_4}(100)$ surface, Phys. Rev. Lett. **107**, 036102 (2011).

[50] M. K. Rasmussen, A. S. Foster, F. F. Canova, B. Hinnemann, S. Helveg, K. Meinander, F. Besenbacher, and J. V. Lauritsen, Noncontact atomic force microscopy imaging of atomic structure and cation defects of the polar $\mathrm{MgAl_2O_4}(100)$ surface: Experiments and first-principles simulations, Phys. Rev. B **84**, 235419 (2011).

[51] J. Bamidele, Y. Kinoshita, R. Turanský, S. H. Lee, Y. Naitoh, Y. J. Li, Y. Sugawara, I. Štich, and L. Kantorovich, Chemical tip fingerprinting in scanning probe microscopy of an oxidized Cu(110) surface, Phys. Rev. B **86**, 155422 (2012).

[52] D. Katsube, R. Shimizu, Y. Sugimoto, T. Hitosugi, and M. Abe, Identification of OH groups on $\mathrm{SrTiO_3}(100)\text{-}(13 \times 13)\text{-}R33.7^\circ$ reconstructed surface by non-contact atomic force microscopy and scanning tunneling microscopy, Appl. Phys. Lett. **122**, 071602 (2023).

[53] R. F. Bader, *Atoms in Molecules: A Quantum Theory* (Oxford University Press, UK, 1990).

[54] F. M. Leibsle, C. F. J. Flipse, and A. W. Robinson, Structure of the Cu{100}-C(2×2)N surface: A scanning-tunneling-microscopy study, Phys. Rev. B **47**, 15865 (1993).